Icing wind tunnel tests of a 15” propeller on altitude

Iris David Du Mutel de Pierrepont Franzetti, Eurac Research, Bolzano, Italy
Federica Sapone, Politecnico di Milano, Milano, Italy
Giuseppe Quaranta, Politecnico di Milano, Milano, Italy
Matteo Mirafiori, Eurac Research, Bolzano, Italy
Riccardo Parin, Eurac Research, Bolzano, Italy

Abstract

In alpine environments, the performance of uncrewed aerial vehicles (UAVs) can be significantly affected by variations in air density associated with high-altitude conditions. Additionally, the combination of high humidity and low temperatures can lead to ice formation and accretion on the propellers, potentially compromising mission success. In this study, we adopt a single-rotor experimental approach to investigate the combined effects of altitude and icing conditions on key performance indicators of an ad-hoc version of a commercially available UAV propeller. Experiments are conducted inside a climatic chamber, with the temperature set to -2 °C and -14 °C to induce the formation of the two most distinct natural ice types: rime and glaze ice. To reduce variability, the cloud droplet size and liquid water content are kept constant throughout the tests. A constant throttle command is applied to the motor, and key performance variables such as thrust, torque, and electrical current are continuously monitored.

1. NOTATION

Symbols:

c_T	Thrust coefficient [-]
c_Q	Torque coefficient [-]
D	Rotor diameter [m]
L	Charachteristic length scale
n	Rotor speed [rev/min]
P_E	Electric power [W]
P_M	Mechanical power [W]
Q	Torque [Nm]
R	Rotor radius [m]
Re	Reynolds number [-]
T	Thrust [N]
μ	Dynamic air viscosity [N·s/m^2]
ω	Rotor speed [rad/s]
ρ	Air density [kg/m^3]

Acronyms:

FoM	Figure of merit [-]
F/T sensor	Force-torque sensor
IWT	Icing wind tunnel
LWC	Liquid water content [g/m^3]
MVD	Median Volume Droplet [μm]
RWUAV	Rotrary wing uncrewed air vehicle
UAS	Uncrewed air system
UAV	Uncrewed air vehicle

2. INTRODUCTION

The involvement of Uncrewed Aerial Systems (UAS) in search and rescue tasks has been increasing in the last decade [1], as these platforms allow for a faster action being capable of carrying a payload containing vital devices and antidotes [2].

Mountain regions are frequently affected by fog conditions and low temperatures, creating challenging icing conditions for rotorcraft flights. In addition, the lower air density caused by altitude affects the performance and autonomy of these vehicles, making the operation exceptionally challenging [3]. Also in northern European countries, UAS operation could be limited to partial times of the year [4] due to icing conditions, challenging the functionality of most UAV applications in those areas.

The propeller ice accretion process has been studied in literature for large scale aircraft [5] and small-scale rotorcraft [6]. Due to the lack of testing facilities, UAV ice accretion processes and their impact on multirotor performance are often studied through a numerical [7], [8] approach. Ice accretion processes have been mainly studied for high Reynolds number conditions [9], [10] as it is a common phenomenon for commercial aircraft, frequently managed using Active Ice protection Systems (AIPS). Rotary wing UAVs (RWUAV), especially multirotors lack the possibility of integrating such solutions, leaving these platforms with no protection against icing conditions. Passive solutions are being sought [11], [12], emphasizing the need for accurate data regarding surface characterization and UAV performance. An icing wind tunnel was used in [13] for the evaluation of two icephobic coatings applied to a scaled version of the Bell Flight APT 70 propellers, where performance degradation was unsuccessfully prevented.

A low-Reynolds setting has been studied operating at low rotor speeds in [14], where lowering the rotation speed was stated to increase the ice accumulation, as a faster speed would cause some of the droplets to pass by the profile due to the faster moving airflow. In [15], a temperature between -4 °C and -10 °C and a high LWC value are stated to be the most dangerous icing conditions for RWUAV performance. According to existing literature, low-adhesion surface coatings, though not superhydrophobic, are considered the most promising solution for icing conditions.

Figure 1 – Test setup and icing wind tunnel

In this work, we present an icing wind tunnel (IWT) campaign on a 15” propeller where both glaze and rime conditions have been tested at different altitudes. The functionality of the IWT described in [16] has been successfully verified under high-altitude conditions, with tests conducted up to an altitude of 6000 meters. This work was preceded by the activities in [6], in which icing conditions for medium scale multirotors were addressed. The assessment of liquid water content (LWC) and median volume diameter (MVD) over the formation of ice on propellers was analyzed, also observing the performance degradation of the single rotor as well as a full quadcopter UAV in terms of thrust and absorbed power.

3. METHODOLOGY

The tests were performed inside the large environmental chamber (LEC) at terraXcube, Eurac Research, Bolzano [17]. The LEC test section has internal dimensions of 12 m × 6 m × 5 m (L × W × H). The IWT was placed inside the chamber, with a single rotor fixed at 1 m from the outlet (see Figure 1). The IWT has been previously characterized by following the guidelines in [18], so that the desired LWC and MVD are reached given a certain air pressure, water pressure and airspeed. A constant LWC of 0.4 g/m^3 and MVD of 35 μm have been set for all the experiments, with an imposed average airspeed of the wind of 5 m/s, water pressure of 3.4 bar and air pressure of 3.4 bar. Two different temperatures, -2 °C and -14 °C, were analyzed for the formation of the two main ice types: glaze ice and rime ice, respectively. The altitudes tested can be found in Table 1.

Table 1 - Test temperature values and ice weight

T_{test} [°C]	Altitude [m]	$T_{chamber}$ [°C]	T_{outlet} [°C]	Ice weight [g]
-2	262	-2	0.3	11.74
	2000	-2.1	0.4	9.43
	3000	-1.9	0.5	8.44
	4000	-1.9	0.2	9.47
	6000	-2.4	-1.3	5.07*
-14	262	-13.9	-10.3	16.22*
	2000	-13.7	-11.1	14.28*
	3000	-14	-11.4	13.15*
	4000	-13.8	-11.7	27.99
	6000	-13.6	-11.4	10.98*

3.1. Setup

The IWT is made up of a 5-meter-long tunnel with a 1 m diameter circular section. At the inlet, a fan collects the air and accelerates it through the tunnel. In front of the fan, a set of 24 nozzles are homogeneously placed on the tunnel section. For all tests present in this work, only two nozzles were used to achieve the desired LWC.

Figure 2 – Icing wind tunnel insides

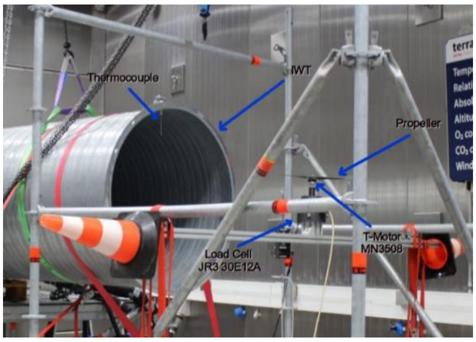

Figure 3 - Setup components and placement

3.2. Sensors

The LEC is equipped with temperature, pressure and humidity sensors to measure the environmental parameters and provide feedback signals for the atmosphere control. Force and torque measurements were obtained using the JR3 30E12A4 load cell, a multi-axis cylindrically shaped monolithic sensor. This device has 6 degrees of freedom. The sensor's z-axis is aligned with the motor's rotational axis. The sensor measurement range is (±200 N, ±200 N, ±400 N) for the forces F_x, F_y and F_z, respectively and ±16 Nm for the torques. The digital resolution is (±0.025 N, ±0.025 N, ±0.050 N) for the forces and ±0.002 Nm for the torques with a stated accuracy of 0.25%. The sensor's operating temperature range goes from −40°C to 65°C. All the measurements were taken in digital mode with a sampling frequency of 10 Hz.

The current and voltage supplied to the motor were logged for the assessment of the efficiency using Ipetronik M-SENS 2 sensor. The maximum voltage measurement range is ±100 V with a stated accuracy of ±0.13% at 25 °C. The current measurement range goes from 0 mA to ±20 mA with a stated accuracy of ±0.30% at 25 °C. All the measurements were taken with a sampling frequency of 10 Hz.

A Hobbywing RPM sensor was connected to two of the phases of the motor for the estimation of the rotor speed. The sensor working temperature range goes from 0°C to 50 °C. The temperature at the tunnel outlet was measured using a thermocouple. While all the sensors were placed inside the test chamber, alongside the micro-controller, all data is transferred through cables and processed from the control room. Both the RPM sensor and the load cell were thermally isolated and enclosed to prevent their malfunction. The sensor placement can be seen in Figure 3.

3.3. Propeller design

All experiments have been performed using a 3D printed model based on the T-Motor Polish 15”x5” carbon fiber propeller used frequently in literature [19], [20]. The propeller was manufactured through a Selective Laser Sintering (SLS) process. The material used is Windform® XT 2.0, a polyamide-based carbon fiber reinforced composite. The propeller has a diameter of 381 mm and a chord of 27.02 mm at 75% of the propeller span. The geometry is modified with a minimum thickness of 0.8 mm to meet the manufacturing requirements. In Figure 4, the CAD design can be seen:

(a) (b)

Figure 4 – Propeller CAD design

The propeller was tested in conditions similar to [19] in order to assess the performance differences with respect to the T-Motor Polish 15”x5” carbon fiber propeller. For a precise evaluation of the most significant differences, experimental data are compared in terms of thrust and torque coefficients (as in equations (1) and (2)) at equal Reynolds number conditions. Results are shown in Figure *5*, showing a good level of agreement. It is to be noted that, while both the current work and [10] exhibit a similar behavior with Reynolds number, the thrust and torque coefficients from [19] are slightly lower. A 6.62% average difference is obtained for the thrust coefficient whereas for the torque coefficient the average difference reaches a 8.64%. The reason behind this may be due to the fact that the baseline propeller used in the present work is manufactured based on a 3D scan of the original propeller obtained in [19]. In addition to a possibly different surface finish, the propeller used in this work has a thicker trailing edge of 0.8 mm, a requirement due to printing constraints.

$$c_T = \frac{T}{1/2\rho n^2 D^4} \quad (1)$$

$$c_Q = \frac{Q}{1/2\rho n^2 D^5} \quad (2)$$

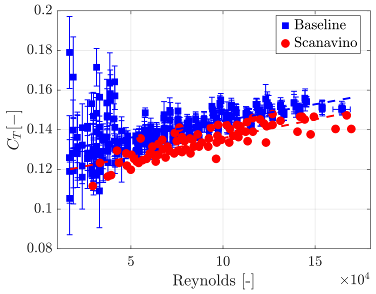

(a)

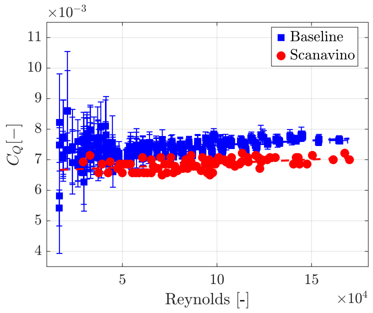

(b)

Figure 5 – Baseline – real propeller comparison: (a) thrust coefficient and (b) torque coefficient

3.4. Testing procedure

Each test consisted of 3 minute runs of a single rotor at a constant throttle command of 50%. The motor used is the T-Motor MN3508, powered at 22.2 V. A power supply was utilized to provide a consistent voltage, which conventional batteries cannot ensure. The propeller was mounted and gradually accelerated to the desired rotational speed. Subsequently, airflow and air pressure within the tunnel were activated, slightly increasing the generated thrust. Once steady-state airflow conditions were reached, the water injection system was activated and let run for approximately 3 minutes. At the end of each test, both the rotor and the IWT were shut down to precisely limit the ice accretion process.

Electric power, thrust, torque and rotation speeds are recorded for every test, granting performance information for each scenario. At the end of each test, the accumulated ice weight was measured using a precision weighing scale as reported in Table 1.

The effective test duration has an average of 150–200 seconds. In cases where ice shedding occurred during the test, the duration was limited as a result. For a precise evaluation of ice formation across different altitudes, a consistent ice growth was sought, enabling accurate measurements of mass and subsequent estimation of ice density. Additionally, assessing the placement and shape of the ice becomes more difficult after partial break-off, which compromises the integrity of the structure. Even if this phenomenon could be caused by the altitude difference by affecting some of the ice characteristics, all tests were stopped shortly after a shedding event took place.

4. EXPERIMENTAL RESULTS

In this section, data post-processing and results are gathered. The impact of ice accretion is presented based on: estimated ice density, raw sensor data and aerodynamic efficiency metrics.

4.1. Ice density estimation

Estimating ice density is valuable for identifying potential differences in the ice formation process that may result from altitude variations. The ice mass is determined by weighing the propellers before and after each test.

The ice volume is estimated using image analysis, as illustrated in Figure 6. Ice thickness is measured with the aid of a reference ruler positioned alongside the propellers in the images.

For the underside of the propellers under rime ice conditions, the ice thickness was estimated based on a 3D scan from an equivalent test performed during a previous campaign. Estimated values of ice density are reported in Table 2, categorized by altitude and temperature.

According to [21] and [22], the densities estimated confirm the classification of the ice types tested as glaze and rime ice. While temperature is the main cause of the ice type differentiation, no substantial differences were found between same ice type densities based on test altitude.

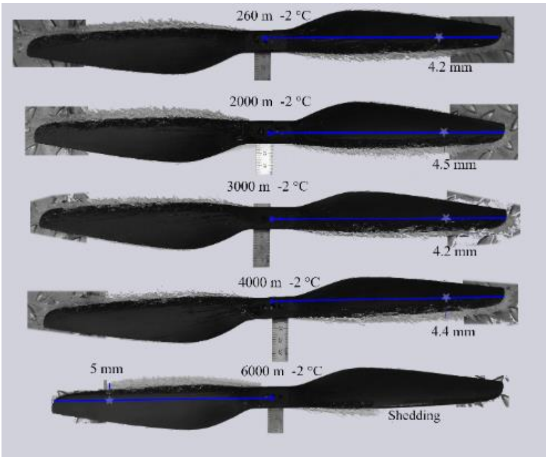

(a)

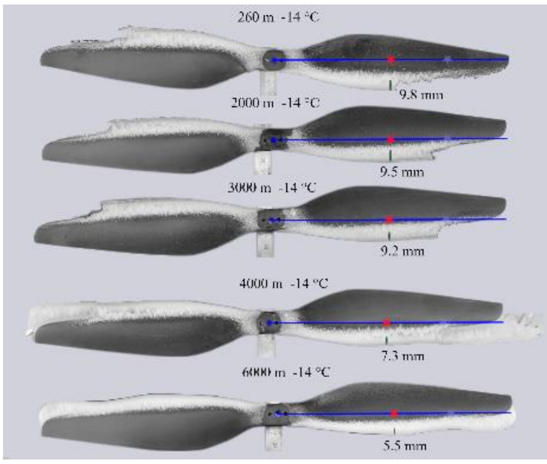

(b)

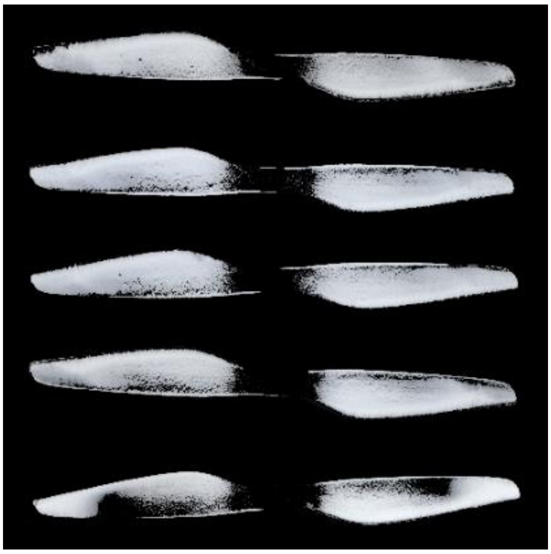

(c)

Figure 6 – Ice formation status at the end of each test at (a) -2 °C, (b) -14 °C front and (c) -14 °C back.

The temperature at the exit of the tunnel is reported in Table 1 to state the possible discrepancies with respect to the reported average temperature which is closer to the main chamber temperature.

Table 2 - Ice density estimation

		Temperature [° C]	
		-2	**-14**
Altitude [m]	**262**	0.62	0.35
	2000	0.72	0.39
	3000	0.98	0.26
	4000	0.78	0.37
	6000	0.87	0.29

4.2. Force-torque data

The data presented in Figure 7 and Figure 8 display the thrust, torque, current draw and rotor speed gathered with the F/T sensor, the Ipetronik system and the Hobbywing speed sensor, respectively. The data is shown from the start of the icing conditions.

All tests have been cropped to isolate the icing effects starting from the activation of the icing wind tunnel. In Figure 7 and Figure 8 all test data shown has been minimally processed to show direct sensor outcome.

As observed in both temperature test cases, the rotation speed increases with altitude. This behavior is expected due to the reduction in air density at higher altitudes. Conversely, the absorbed current decreases, which is also a consequence of the lower air density. Thrust and rotor torque both decline with altitude, reflecting well-known aerodynamic effects associated with operating in thinner air.

In the data shown in these figures, the impact of both altitude and ice accretion is presented. Since absolute values are being compared, the combined influence of air density and ice buildup can be directly observed. The data obtained at -2 °C presents unperturbed behavior coming from all sensors, being reliable for the performance evaluation of the rotor under such conditions. On the other hand, the load cell produced unexpected results during the lowest temperature tests reflecting a sensor malfunction. Only electric power and rotation speed are available and suitable for further analysis. For this reason, results involving load cell data at -14 °C have been discarded, showing information from the remaining reliable sensors as an assessment of the rotor performance. For glaze ice, shedding was observed only during the test conducted at 6000 m. In contrast, during rime ice conditions, ice detachment was detected at 262 m, 2000 m, and 3000 m, as indicated by anomalies in the current and rotor speed data.

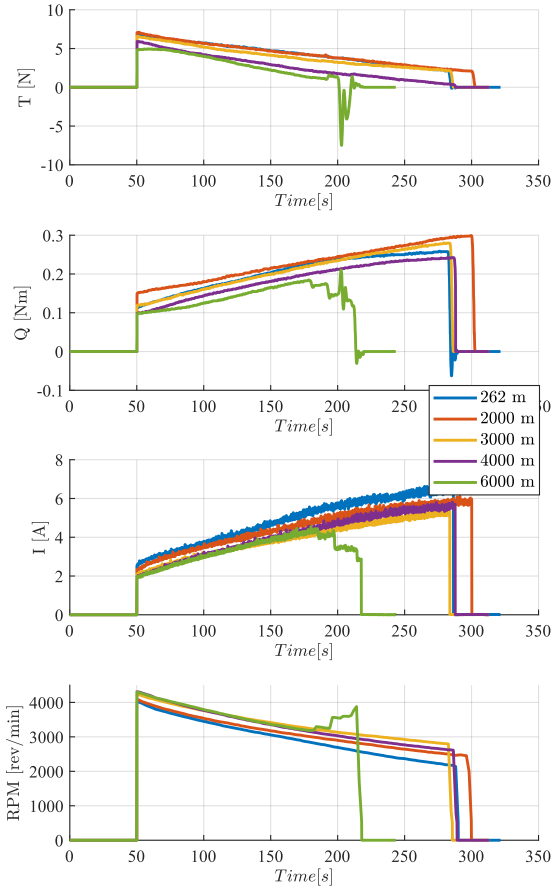

Figure 7 – Raw data for glaze icing conditions

At 4000 m, a total of 27.99 g of ice accumulated (see Table 1) without triggering any shedding, despite the exposure to icing conditions lasting longer than in the two lower-altitude tests. At 6000 m, the ice formation appears to have a less disruptive effect on the propeller's rotation, based on both current and tachometer measurements. Similarly, the data from the 4000 m test shows a trend comparable to the lower altitude cases but with more favorable behavior in terms of rotational speed and current draw.

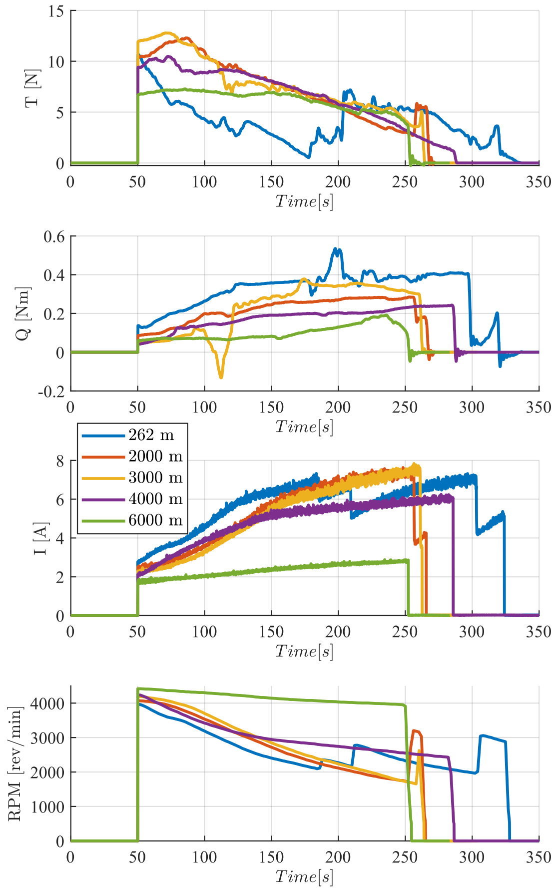

Figure 8 – Raw data for rime icing conditions

In Figure 9, the mechanical power for glaze ice conditions is shown. This parameter has been computed as:

$$P_M = \omega \cdot Q \tag{3}$$

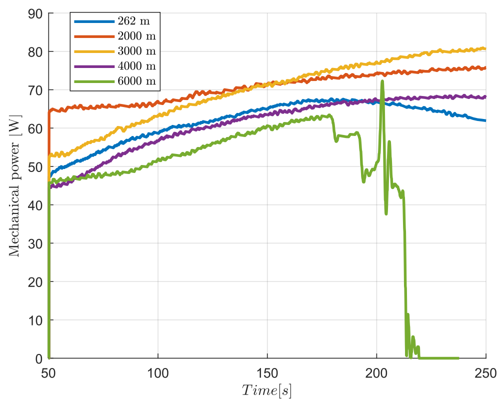

Figure 9 - Mechanical power under glaze ice conditions (-2 °C)

No definitive conclusions can be drawn from these results, as both altitude and ice formation simultaneously influence the measured parameters. To enable a more meaningful comparison between tests and to isolate the effects of ice accretion, it is proposed to normalize the test data by the initial absolute values of each parameter. This ratio-based approach helps to reduce the impact of varying air density conditions and focuses on the influence of ice buildup alone.

4.3. Performance evaluation

In this section, the performance of the rotor is measured using well-known aerodynamic efficiency metrics. In particular, the *Figure of Merit* (*FoM*) and the ω/P_E ratio. The FoM quantifies efficiency by comparing the ideal power required to generate a given thrust with the actual power consumed. Figure *9* presents the FoM (equation (4)) for the tests conducted at –2 °C.

$$FoM = \frac{T^{\frac{3}{2}}}{P_E\sqrt{2\rho A}} \qquad (4)$$

To illustrate the efficiency trend and potential performance degradation over time, the measured FoM during the test is normalized by its initial value.

The absolute FoM values can be recovered by multiplying the normalized data by the initial FoM, which is indicated in the colorbar adjacent to the graph.

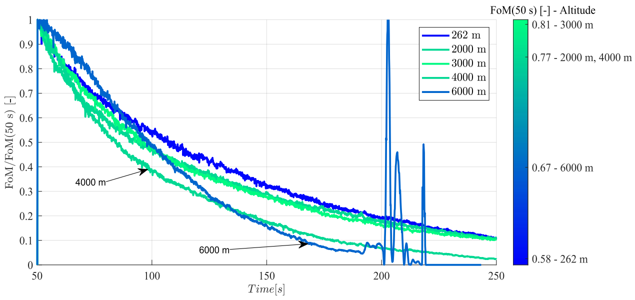

Figure 10 - Figure of merit for tests at -2 °C

As observed from the color bar presented next to the graph, the lowest initial Figure of Merit (FoM) value is observed at 262 m, corresponding to the highest air density condition. In this scenario, the rotor absorbs more power due to the increased aerodynamic loading. Overall, the FoM ratio follows a consistent trend across all altitudes with a decrease of 90% of its initial value, with 4000 m and 6000 m tests performing even worse with a degradation of 98% of the initial FoM. At 4000 m, a more rapid decline in FoM is observed compared to the lower altitude tests. The 6000 m test displays the poorest performance, reaching the lowest FoM ratio values. Notably, ice shedding occurs only at 6000 m, which introduces additional variability and noise into the FoM after second 200. The analysis of the FoM for the -14 °C tests was not viable due to the high noise present in the recorded thrust data.

In Figure 11, the efficiency of all tests is analyzed presenting the $\frac{\omega}{P_E}/\frac{\omega}{P_E}(50s)$ relationship with each absolute initial value presented in the colorbar next to the corresponding graph.

The $\frac{\omega}{P_E}$ metric is used to assess efficiency independently of the F/T sensor. In Figure 11(a), the -2 °C scenario is shown, where all tests exhibit a steady decline over time of 70% of the corresponding initial values. As observed previously, the 6000 m case shows a shedding event, which temporarily reestablishes the ratio to a 50% of the initial value before the end of the test.

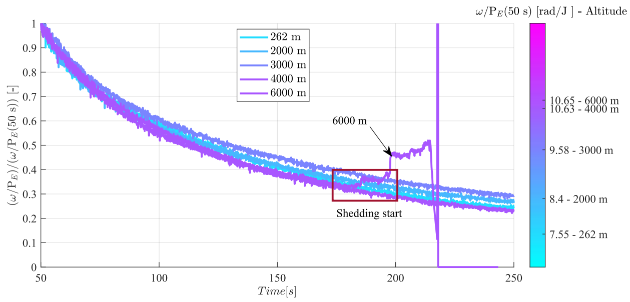

(a)

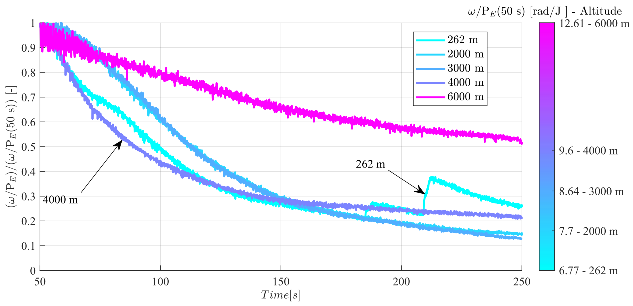

(b)

Figure 11 – Rotor speed over electric power (ω/P_E) [rad/J] for tests at (a) -2 °C and (b) -14 °C

At -14 °C the highest initial $\frac{\omega}{P_E}$ value is observed for 6000 m, with values decreasing with altitude. However, the rate of decline becomes less steep at higher altitudes: the 6000 m test reaches a ratio of 60% of the initial value at the second 200. Following this is the 4000 m test, which undergoes a sharp initial descent before reaching a 0.25 ratio at 200 seconds. The remaining altitudes stay below these values after 150 seconds, except for 262 m, where two notable shedding events occur, resulting in a recovery in the $\frac{\omega}{P_E}$ ratio of approximately 10% after 180 seconds. The use of ratios to compare the performance of the same rotor under varying environmental conditions enables a clear visualization of performance trends over time. An effective comparison among tests can be performed regarding ice effect on rotor performance.

Although the data presented in Figure 11 does not include thrust or torque information which could be important for determining the hovering and maneuvering capabilities of a hypothetical rotorcraft, it effectively highlights the impact of ice accretion on rotor speed, effectively serving as an indicator for ice blockage of the rotor.

The effect of altitude on ice formation remains unclear and inconclusive, as no consistent differences were observed in either the amount of ice accreted or the estimated ice density. However, as shown in Figure 6(c), rime ice accumulation on the underside of the propeller blades presents changes with increasing altitude. A possible explanation for this behavior is a variation in ice morphology or placement given by a lower pressure setting.

5. CONCLUSIONS

Single rotor experiments have been completed at two different temperatures and five different altitudes to analyze the two main ice formations for rotorcraft: rime and glaze ice. Different altitudes are simulated to further increase the similarities with a real flight through a high humidity scenario. A custom propeller was manufactured for the characterization of the material, which is frequently used in the development of aerospace hardware. Results regarding total thrust, torque, electric power, rotor speed as well as icing wind tunnel configuration have been recorded for each test. Additionally, the ice accretion is quantified by measuring the ice mass at the end of each run. Performance for every scenario was evaluated based on the available data, and ice density was estimated in all cases to support further comparison and analysis of ice formation differences. The novelty of this work lies in the evaluation of rotorcraft performance under realistic icing conditions, with a low-density icing environment closely replicating flight under very low Reynolds and high humidity conditions. The study of the characteristics of a 3D printed propeller is also decisive in the development of ad-hoc coating solutions adequate to such surface.

As main outcome of this study, weak differences in the ice formation process were detected for the proposed altitudes and cloud characteristics. In particular, glaze ice presents equivalent behavior at all altitudes tested. Opposed to what is frequently observed, shedding events were more frequently found during rime icing conditions rather than with glaze ice. At 6000 m and -2 °C, ice shedding takes place, whereas under rime ice conditions, shedding was observed at the three lower altitudes, with rotor speed and electric power performance improving as altitude increased. Additionally, for rime ice, a reduction in under-rotor ice accumulation was noted with increasing altitude. The lower air density at higher altitudes appears to positively influence the placement and shape of rime ice, potentially contributing to more favorable accumulation characteristics.

The behavior of the F/T sensor has proven to be unreliable under extreme thermal conditions. As a future improvement of the setup, a protective cover for this sensor should be crafted, blocking completely the penetration of water and ice on the sensor grooves without influencing the sensor measurement capabilities. Alternatively, a different sensor should be proposed. Regarding ice density estimation, a 3D scanning method will be used, granting an accurate measurement of the ice volume.

Figure 12 – Tubercled propeller

The propeller tested in this campaign was previously tested in different air density conditions to fully characterize its performance and compare it to its commercial counterpart. Additionally, an analogous propeller model was made using the same material in which the leading edge has been modified as in Figure 12 aiming at delaying a stall scenario when flying in low density settings. The natural continuation of this line of research will involve the evaluation of these propellers in icing conditions to determine the convenience of this modification.

Author contact:

Iris David Du Mutel de Pierrepont Franzetti iris.daviddumutel@eurac.edu,

Federica Sapone federica.sapone@mail.polimi.it,

Giuseppe Quaranta giuseppe.quaranta@polimi.it,

Matteo Mirafiori matteo.mirafiori@eurac.edu,

Riccardo Parin Riccardo.parin@eurac.edu

6. ACKNOWLEDGMENTS

We would like to thank Andrea Eccher, Alessandro Apolito, Florian Forstner and Carsten Patzelt for their help and support during the test campaign.

7. REFERENCES

[1] Z. Kashino, G. Nejat, and B. Benhabib, “Aerial Wilderness Search and Rescue with Ground Support,” 2019, doi: 10.1007/s10846-019-01105-y/Published.

[2] M. J. van Veelen *et al.*, “Drones reduce the treatment-free interval in search and rescue operations with telemedical support – A randomized controlled trial,” *American Journal of Emergency Medicine*, vol. 66, pp. 40–44, Apr. 2023, doi: 10.1016/j.ajem.2023.01.020.

[3] R. Parin, A. Bojeri, F. Benedetto, G. Ristorto, and G. Guglieri, “Unmanned Aerial Vehicles Experimental Characterization in Controlled Extreme Environmental Conditions,” *2023 International Conference on Unmanned Aircraft Systems, ICUAS 2023*, pp. 658–662, 2023, doi: 10.1109/ICUAS57906.2023.10155932.

[4] T. Lundby, M. P. Christiansen, and K. Jensen, “Towards a weather analysis software framework to improve UAS operational safety,” *2019 International Conference on Unmanned Aircraft Systems, ICUAS 2019*, pp. 1372–1380, Jun. 2019, doi: 10.1109/ICUAS.2019.8798271.

[5] P. H. Von Hardenberg, C. A. Flack, and D. L. Rigby, “Ice Shape Analysis of an eVTOL Propeller in Forward Flight at the NASA Glenn Icing Research Tunnel.”

[6] I. David Du Mutel de Pierrepont Franzetti, A. Avi, E. Capello, G. Quaranta, and R. Parin, “UAV Icing Trials: a new approach,” in *50th European Rotorcraft Forum*, 2024. Accessed: Feb. 27, 2025. [Online]. Available: https://bia.unibz.it/esploro/outputs/conferencePresentation/UAV-Icing-Trials-a-new-approach/991006942224601241

[7] N. C. Müller, R. Hann, and T. Lutz, “UAV Icing: Numerical Simulation of Propeller Ice Accretion,” *AIAA AVIATION 2021 FORUM*, 2021, doi: 10.2514/6.2021-2673.

[8] R. Hann, A. Wenz, K. Gryte, and T. A. Johansen, “Impact of atmospheric icing on UAV aerodynamic performance,” *2017 Workshop on Research, Education and Development of Unmanned Aerial Systems, RED-UAS 2017*, pp. 66–71, Nov. 2017, doi: 10.1109/RED-UAS.2017.8101645.

[9] F. T. Lynch and A. Khodadoust, “Effects of ice accretions on aircraft aerodynamics,” *Progress in Aerospace Sciences*, vol. 37, no. 8, pp. 669–767, Nov. 2001, doi: 10.1016/S0376-0421(01)00018-5.

[10] M. B. Bragg, A. P. Broeren, and L. A. Blumenthal, “Iced-airfoil aerodynamics,” *Progress in Aerospace Sciences*, vol. 41, no. 5, pp. 323–362, Jul. 2005, doi: 10.1016/J.PAEROSCI.2005.07.001.

[11] R. Hann *et al.*, “Experimental Investigations of an Icing Protection System for UAVs,” *SAE Technical Papers*, vol. 2019-June, no. June, Jun. 2019, doi: 10.4271/2019-01-2038.

[12] N. C. Müller, B. Low-Hansen, K. Troller Borup, and R. Hann, “UAV icing: Development of an ice protection system for the propeller of a small UAV,” *Cold Reg Sci Technol*, 2023.

[13] D. Harvey, E. Villeneuve, C. Volat, M. Beland, and M. Lapalme, “Experimental Evaluation of Icephobic Coatings on a UAV Propeller Operated in an Icing Wind Tunnel,” *SAE Technical Papers*, Jun. 2023, doi: 10.4271/2023-01-1443.

[14] E. Villeneuve, A. Samad, C. Volat, M. Béland, and M. Lapalme, “Experimental Investigation of Icing Effects on a Hovering Drone Rotor Performance,” *Drones 2022, Vol. 6, Page 345*, vol. 6, no. 11, p. 345, Nov. 2022, doi: 10.3390/DRONES6110345.

[15] M. Muhammed and M. S. Virk, “Ice Accretion on Rotary-Wing Unmanned Aerial Vehicles—A Review Study,” *Aerospace 2023, Vol. 10, Page 261*, vol. 10, no. 3, p. 261, Mar. 2023, doi: 10.3390/AEROSPACE10030261.

[16] A. Avi, L. Becce, G. Quaranta, F. Mazzetto, and R. Parin, “Characterization of the Spray System of the TerraXcube Icing Wind Tunnel,” *Aerotecnica Missili & Spazio*, Jun. 2024, doi: 10.1007/s42496-024-00224-6.

[17] terraXcube EURAC Research, “Large Cube | terraXcube.” Accessed: Jan. 16, 2025. [Online]. Available: https://terraxcube.eurac.edu/en/large-cube

[18] SAE International, “ARP5905-Calibration and Acceptance of Icing Wind Tunnels,” 2015.

[19] M. Scanavino, S. Giorgio Guglieri, and S. Andrea Vilardi, “Design and testing methodologies for UAVs under extreme environmental conditions.”

[20] C. Russell, G. Willink, C. Theodore, J. Jung, and B. Glasner, “Wind Tunnel and Hover Performance Test Results for Multicopter UAS Vehicles,” 2018. [Online]. Available: http://www.sti.nasa.gov

[21] “Glaze | UNDRR.” Accessed: Jul. 22, 2025. [Online]. Available: https://www.undrr.org/understanding-disaster-risk/terminology/hips/mh0045

[22] “rime - Glossary of Meteorology.” Accessed: Jul. 22, 2025. [Online]. Available: https://glossary.ametsoc.org/wiki/Rime